Electrochemical behavior of drawn thin-film vitreous lithium metaphosphate

*Jacob Wheaton[a], Steven Kmiec[a], Devon Schuler[a], Christopher Sorensen[a], Steve W. Martin[a]**

[a]Department of Materials Science and Engineering, Iowa State University of Science and Technology, 528 Bissell Rd, Ames, IA 50012, United States

*Email: swmartin@iastate.edu

Keywords: Solid-state electrolyte, lithium battery, thin film, ion conduction, oxide glass

ABSTRACT

Lithium metaphosphate ($LiPO_3$) thin-film glassy solid-state electrolyte (GSSE) ribbons with thicknesses varying from 35 to 800 μm have been drawn for the first time through softening and drawing of a cast and annealed preform of $LiPO_3$ glass. The short-range order structure and composition of the thin-film glasses were confirmed to be identical to the bulk glass $LiPO_3$ using Raman spectroscopy. Electrochemical impedance spectroscopy (EIS) was used to investigate the Li ionic conductivity of the thin-film GSSE samples and was essentially the same as that of the bulk $LiPO_3$ glass. A model of area specific resistance (ASR) as a function of film thickness and temperature was generated and compared to resistances determined through equivalent circuit fitting of EIS generated Nyquist plots. The generated model compared well to the experimentally

determined values. Li|GSSE|Li symmetric cell cycling was conducted on the 50 μm thick samples to determine the cycling behavior and the durability of the $LiPO_3$ GSSE in contact with lithium metal (LM) under applied voltage and sustained current. Evidence of electrochemical stability of the $LiPO_3$ thin-film GSSE against LM was observed in the symmetric cell cycling as nearly perfectly flat and ohmic behavior cycling plateaus were found over a range of current densities. Prior to shorting, a critical current density (CCD) of 65 $\mu A/cm^2$ was obtained at 90°C with a D.C. Li ionic conductivity of $10^{-6.5}$ $[\Omega\text{-cm}]^{-1}$. While these current densities are low and consistent with the low D.C. conductivity of this particular GSSE, this is the first report of a thin-film GSSE drawn into thicknesses of that required for high performance all-solid-state lithium batteries (ASSLBs) and the observed proven stability and durability of this oxide GSSE is strong evidence that drawn thin-film GSSE materials, especially those with higher conductivities such as the well-studied sulfide glasses, are viable materials from which to create thin, easily-processable solid-state electrolytes (SSEs), and warrants further research.

Introduction

As electric vehicles and renewable energy sources become more prevalent in the world, novel energy storage materials are required to meet the increasing demand for safe, high energy density batteries[1-3]. Lithium ion batteries have emerged as the dominant battery to meet the needs of this growing trend and have been well studied since their commercialization in 1991[4-8]. Prior to carbon anodes, lithium metal (LM) was utilized as the negative electrode, but it was quickly found prone to lithium dendrite formation, leading to the organic liquid electrolyte (OLE) catching fire[9-11]. The use of graphitic carbon anodes was found to avert the formation of lithium dendrites and allowed for increased safety at the expense of lower energy density[12].

All-solid-state lithium batteries (ASSLBs) utilizing solid-state electrolytes (SSEs) have been investigated for many years in the hope of enabling the use of high specific capacity LM anodes by eliminating the flammable OLE[13]. However, as they appear to have solved some of the problems with using LM anodes, they still present many challenges that have not yet been overcome. Of interest here in this work is the transition from small laboratory-scale production of test quantities of SSEs to the full large-scale manufacturing of quantities that are required at the gigawatt scale[14].

There are several requirements for SSE materials on the laboratory scale. SSEs should have high room temperature ionic conductivities approaching 10^{-3} $[\Omega\text{-cm}]^{-1}$, have extremely low electronic conductivity ($< 10^{-9}$ $[\Omega\text{-cm}]^{-1}$), electrochemical stability at low reducing potentials against LM and at high oxidizing potentials of +5 V against high voltage cathodes[15-17]. A high ionic conductivity is important to achieve low overpotentials on the SSE, and to allow for faster charge and discharge rates, while a low electronic conductivity is desirable to prevent parasitic loss of charge over time and dendrite formation[18]. The electrochemical stability window, 0 to +5 V vs Li/Li^+, is important

to prevent side reactions from occurring at both the anode and cathode leading to cycle fatigue and lower coulombic efficiencies. As some SSEs are beginning to meet all of these requirements on the laboratory scale, it is now becoming important to look towards ultimate scale-up and commercialization processes that will be necessary for any SSE to meet gigawatt scale requirements. It is to this aspect of SSE development that this work is directed.

Some requirements for scaling-up of laboratory technology are the cost, ease-of-manufacture, and the quality of SSE that can be obtained. The main processing methods for inorganic polycrystalline ceramic SSEs are tape casting, atomic layer deposition (ALD), chemical and physical vapor deposition (CVD and PVD), and melt processing[14, 19-21]. While tape casting and melt processing are very common ceramic processing techniques, ALD, CVD, PVD, and other film growth techniques are often relatively high cost and low throughput[16, 22]. Tape casting often requires burning out of binders and further densification and sintering of the ceramic particles, often at high temperatures for long periods of time[22]. Melt processing can be a challenging technique due to the high melting temperatures (>1000°C) of most oxide-based ceramic SSEs. It is important to note that the choice of material is often the single most limiting factor for the available processing options.

While there are several types of SSEs, this work will focus on that of inorganic glasses. Glassy SSEs (GSSEs) have been shown to possess higher conductivities than their crystalline analogues[23-24]. The intrinsic lack of grain boundaries in monolithic GSSEs and their highly tunable chemistries make them good candidates for use as SSEs[25]. Many GSSEs also possess modest melting temperatures (<900°C) and viscous flow behavior at low temperatures (<350°C), allowing for relatively easy processing[26-27]. While pure oxide GSSEs were the first to be investigated nearly 100 years ago, their Li and Na ionic conductivities are rarely above 10^{-6} $[\Omega\text{-cm}]^{-1}$, several orders

of magnitude lower than desired[28-29]. Sulfide GSSEs have been shown to possess conductivities approaching 10^{-3} $[\Omega\text{-cm}]^{-1}$, but are often unstable in atmosphere or against LM[30-33]. Mixed oxy-sulfide glasses have been shown to possess qualities of both the oxide and the sulfide, being both stable in air and against LM, while still possessing the high conductivities of the sulfide glass[34-35].

While these studies described above have been conducted on the compositional exploration of new SSEs, improving their processability into the thin films of ≈ 20 to 50 μm needed for cell performance is still under development[36]. While increasing cell energy density is one of the largest driving forces for decreasing the electrolyte thickness, low cell resistance is also necessary to be able to reduce loss across the electrolyte. In order to achieve the lowest possible SSE resistance, variables must be considered in addition to material selection, such as electrolyte geometry, which is often limited by the properties and available processing techniques of the material itself.

Sample geometry is one way to further lower SSE resistance while keeping the electrolyte material constant. The resistance (R) of an electrolyte can be geometrically described through Eq. (1), where t is the sample thickness, A is the sample area, and σ is the conductivity of the material.

$$R = \frac{t}{A\sigma} \ [\Omega] \quad \text{Eq. (1)}$$

The area of the electrolyte is determined by the geometry of the desired application, while the thickness is generally determined by the processing of the material. As cell sizes are highly dependent on the application, it is often desirable to compare the area specific resistance (ASR) of a material, which is normalized to a unit area and described through a minor modification to Eq. (1), as shown in Eq. (2).

$$ASR = RA = \frac{t}{\sigma} \ [\Omega\text{-cm}^2] \qquad \text{Eq. (2)}$$

The ASR allows for easier comparison of the resistance of cells as it considers the intrinsic conductivity and the thickness of the electrolyte separator. From Eq. (2), it can be seen that ASR decreases linearly with decreasing thickness and constant conductivity. Thus, decreasing the thickness of the electrolyte from ≈ 1 mm to 100 μm would decrease the resistance by an order of magnitude. At a conductivity of ≈ 10^{-3} [Ω-cm]$^{-1}$, films < 100 μm are necessary to be competitive with organic liquid electrolytes[14].

GSSEs are unique in their processability due to their viscoelastic behavior above the glass transition temperature (*Tg*). In much the same way as glass fibers are made, with different sized bulk glass preforms and an appropriately designed drawing apparatus, it is possible to cast and anneal a large quantity of glass, and then reheat this preform to just above the *Tg* and into the viscoelastic supercooled liquid state and draw out thin-film glass ribbons in a facile and repeatable manner. While twin-roller quenching can generate thin-film glasses as well, these films have small dimensions that are more similar to flakes than to full sheets and are generally pressed into powder compacts to be used[37].

Here we report the first study of a bulk drawn thin-film GSSE and its electrochemical behavior. Due to the similar viscosity behavior and relative ease of manufacture, lithium metaphosphate ($LiPO_3$) was chosen as an analogous glassy material to use as a preliminary investigation into the performance and processing challenges of utilizing drawn thin-film glassy electrolyte materials in battery applications. While $LiPO_3$ exhibits a low ionic conductivity at room temperature of 4.1×10^{-9} [Ω-cm]$^{-1}$, it is an excellent model system for investigating the processing and electrochemical performance of other thin-film fast-ion-conducting glasses[38-39]. The ASR of thin films of $LiPO_3$ was evaluated as a function of thickness and temperature and was shown to decrease linearly with decreasing thickness. This could be accurately modeled through conductivity

measurements of the bulk melt quenched glass. Symmetric cell testing demonstrated that the 50 μm thin film was mechanically durable enough to withstand over 350 cycles at varying temperatures and current densities, with no degradation in cycling behavior prior to short-circuiting. This study acts as a proof-of-concept to demonstrate that thin-film drawn glass is a viable processing method for future, thin, low-resistance solid electrolyte materials.

Experimental Section

Materials Synthesis

Lithium carbonate (Li_2CO_3 99+% Acros Organics) and diammonium phosphate ($(NH_4)_2HPO_4$ 99+% Acros Organics) were used as received for synthesis of $LiPO_3$. Batches of 250 g were prepared by measuring stoichiometric amounts of the raw materials in a fume hood and milled together using a mortar and pestle. The powder was loaded into a porcelain crucible and heated at 200°C for 10 hours to drive off H_2O and NH_3, followed by ramping to 800°C and holding for 3 hours to drive off CO_2 and form a homogenous melt. For small-scale batches, this liquid was then cast into small, 1-cm-wide bars of approximately 15 grams. Melt-quenched (MQ) samples were prepared through remelting of ≈ 7 g batches of these bars and quenching in preheated circular molds in a N_2 glovebox (<5 ppm O_2 and H_2O), followed by annealing below the *Tg* at 290°C for three hours. A differential scanning calorimetry thermogram for $LiPO_3$ is shown in Figure S1 to show the glass transition temperature.

For the large preform, the liquid was created as above and cast onto a preheated brass plate, covered with a second preheated brass plate, and then annealed at 290°C overnight to form a rectangular preform approximately 10 cm by 25 cm by 1 cm. [40]. After cooling, the preform was loaded into our custom-built thin film draw tower located inside of a N_2 glove box (<0.1 ppm O_2 and H_2O). A schematic of the draw-tower is shown in Figure 1. The preform is loaded into the

preform feeding system and is lowered into the upper zone of the furnace where the temperatures are highest such that only the tip of the glass preform is heated. The glass is then heated slowly to around 340-360°C where it softens, elongates, and then stretched into the tractor system below the furnace which then maintains a constant pulling speed. Several processing variables can be adjusted to achieve film thicknesses between 20 and 800 μm. These variables include the preform feed speed, the tractor speed, the furnace upper zone temperature, and the furnace lower zone temperature. The starting values for the preform feed speed and the tractor speed were 0.90 mm/min and 100 mm/min, respectively. These values are adjusted up or down slightly depending on the behavior and thickness of the film being drawn. As all of these variables affect the film drawing, they must be simultaneously optimized to create optimum draw conditions.

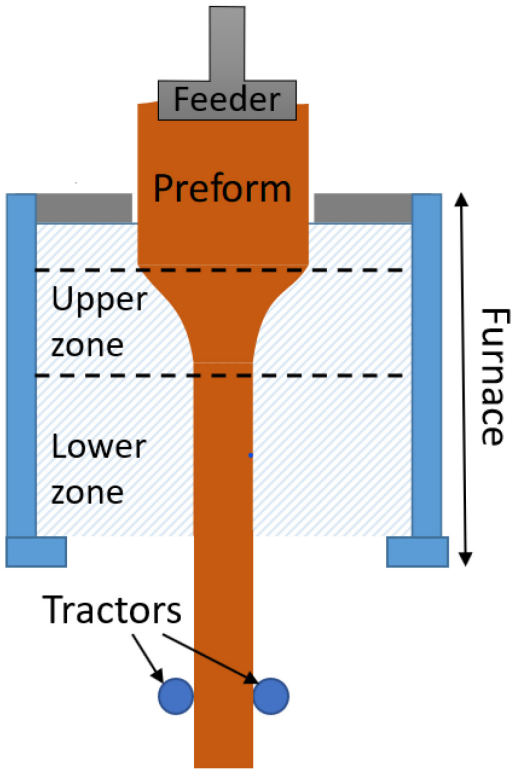

Figure 1. Side view schematic of the draw tower, showing the preform loaded into the preform feeder, the hot upper zone, the lower temperature lower zone and the tractors that create tension on the film to consistently pull ribbons.

Large ribbons (approximately 10 cm by 50 cm) were generated through the drawing process as seen in Figure 2a. Consistent with the report by O'Kiely *et al.*[41], the glass ribbons exhibit a degree of edge thickening; however, they do show a large steady-state central region with minimal changes in thickness, as shown in Figure 2c. The glass sheets were cut into samples with areas of < 1 cm^2 for further testing, avoiding using any of the thickened edges. A sample piece of film used in a symmetric cell is shown in Figure 2b. Pieces of film that were too small for use in cells and the removed thick edges were collected and remelted or used as cullet in new batches. Several different preforms were drawn under different pulling conditions in order to generate the films tested in this study.

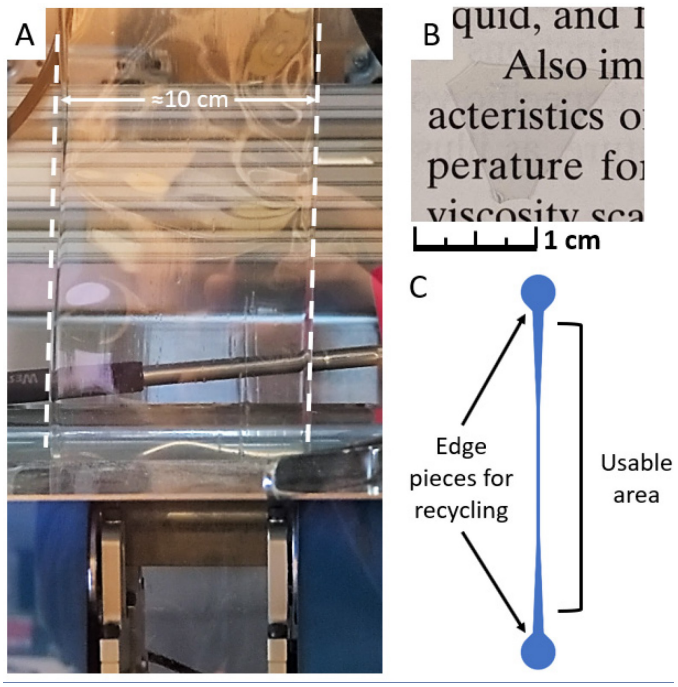

Figure 2. (a) Image of a sheet of $LiPO_3$ film approximately 10 cm in width in the process of being drawn. The dotted white lines are shown to highlight the edge of the glass sheet. **(b)** An image of a 45 µm thin film for use in symmetric cells, the small ruler in the corner shows a total length of 1 cm. **(c)** Diagram of a width cross-section of a drawn thin-film glass sheet showing the usable area and the recyclable thick edge pieces.

Raman Spectroscopy

In order to confirm the composition, samples were removed from the glove box and tested quickly to prevent reaction of the glass with the humidity in the air. Spectra were collected using an inVia 488 nm Renishaw Coherent Laser Raman Spectrometer which was calibrated to an internal standard silicon reference centered at 520 ± 0.5 cm^{-1}. Samples were tested under a 20x objective lens, with a spot size of ≈ (50 μm)^2, from 100 cm^{-1} to 2000 cm^{-1} with 20 accumulations at 12.5 mW power. The Raman spectra so collected are presented in Figure S2, with peak assignments listed in the Supplemental Information.

Ionic Conductivity

MQ cast disk samples of 15 mm diameter were prepared for conductivity testing by dry polishing to ≈ 1 μm followed by gold sputtering 10 mm diameter electrodes using an Anatech Hummer VI Sputtering System. Samples were packed into a custom airtight sample holder. Thin film cells were prepared in symmetric cell LM | $LiPO_3$ | LM CR2032 coin cells with electrode areas under 1 cm^2. No polishing was needed for the thin-film cells due to the naturally smooth surface of the film. Ionic conductivity was measured using a Novocontrol 2 Dielectric Spectrometer with a cryostat enabling temperature measurements between -100°C and 300°C. Electrochemical impedance spectroscopy (EIS) measurements of the MQ glass disks were taken from -45°C to 200°C between the frequency range of 7 MHz to 0.1 Hz. Typical EIS Nyquist plots are presented in Figure 3a for MQ bulk $LiPO_3$ GSSE.

Symmetric cells of thin-film $LiPO_3$ GSSE were tested in the same frequency range to determine the ionic conductivity as a function of temperature from -45°C to 120°C. The Nyquist plots were fitted using the equivalent circuit model shown in Figure 3b. Fitted resistance values were used to determine ionic conductivity using Eq. (3), where $\sigma(T)$ is the temperature dependent ionic

conductivity, t is the electrolyte thickness, $R_{bulk}(T)$ is the temperature dependent resistance, and A is the area. Thickness was measured by averaging at least five different measurements with a micrometer. The activation energy $\left(\Delta E_a\right)$ was determined using the modified Arrhenius function shown in Eq. (4), where σ_0 is the pre-exponential factor, T is the absolute temperature, and R is the ideal gas constant.

$$\sigma(T) = \frac{t}{R_{bulk}(T)A} \ [\Omega\text{-cm}]^{-1} \quad \text{Eq. (3)}$$

$$\sigma(T) = \frac{\sigma_0}{T}\exp\left(\frac{-\Delta E_a}{RT}\right) \ [\Omega\text{-cm}]^{1} \qquad \text{Eq. (4)}$$

Electrochemical Characterization

Time dependent EIS and galvanostatic cycling were conducted using a Biologic VMP-300 potentiostat. Cells were fabricated inside an Ar glovebox (<0.1 ppm O_2 and H_2O) using Li | $LiPO_3$ | Li inside of CR2032 type coin cells with electrode areas less than 1 cm^2. EIS scans were collected every 30 minutes for approximately 24 hours from 7 MHz to 0.1 Hz with a 0.5 V sinus amplitude. Following the EIS scans, low current density cycling was conducted at room temperature (≈ 20°C), 60°C, and 90°C. The critical current density (CCD) was determined through step increasing the current at the end of a cycle until either the cell shorted, or the voltage limit of the potentiostat was reached (± 10 V).

Results and Discussion

Ionic Conductivity - Modeling Resistance as a Function of Thickness

The Nyquist plots determined through EIS were analyzed and fitted using the circuit shown in Figure 3b. A few examples of the Nyquist plots are shown in Figure 3a and the temperature dependent D.C. ionic conductivity is shown in Figure 3b. The extracted bulk resistance values were used to determine the temperature dependent conductivity, which follows an Arrhenius relation. The room temperature ionic conductivity was determined to be $1.8 \cdot 10^{-9} \pm 0.3 \cdot 10^{-9}$ $[\Omega\text{-cm}]^{-1}$. This is close to the literature values of $2.5 \cdot 10^{-9}$ $[\Omega\text{-cm}]^{-1}$ reported by Wang *et al.* for $Li_{0.92}PO_{2.96}$[42] and $2.4 \cdot 10^{-9}$ $[\Omega\text{-cm}]^{-1}$ reported by Martin and Angell for $LiPO_3$[43]. Linear fitting ($R^2 = 0.9998$) of the Arrhenius function shows that the activation energy for conduction was determined to be 71.5 ± 0.2 kJ/mol which agrees well with the literature value of 70.9 kJ/mol[44].

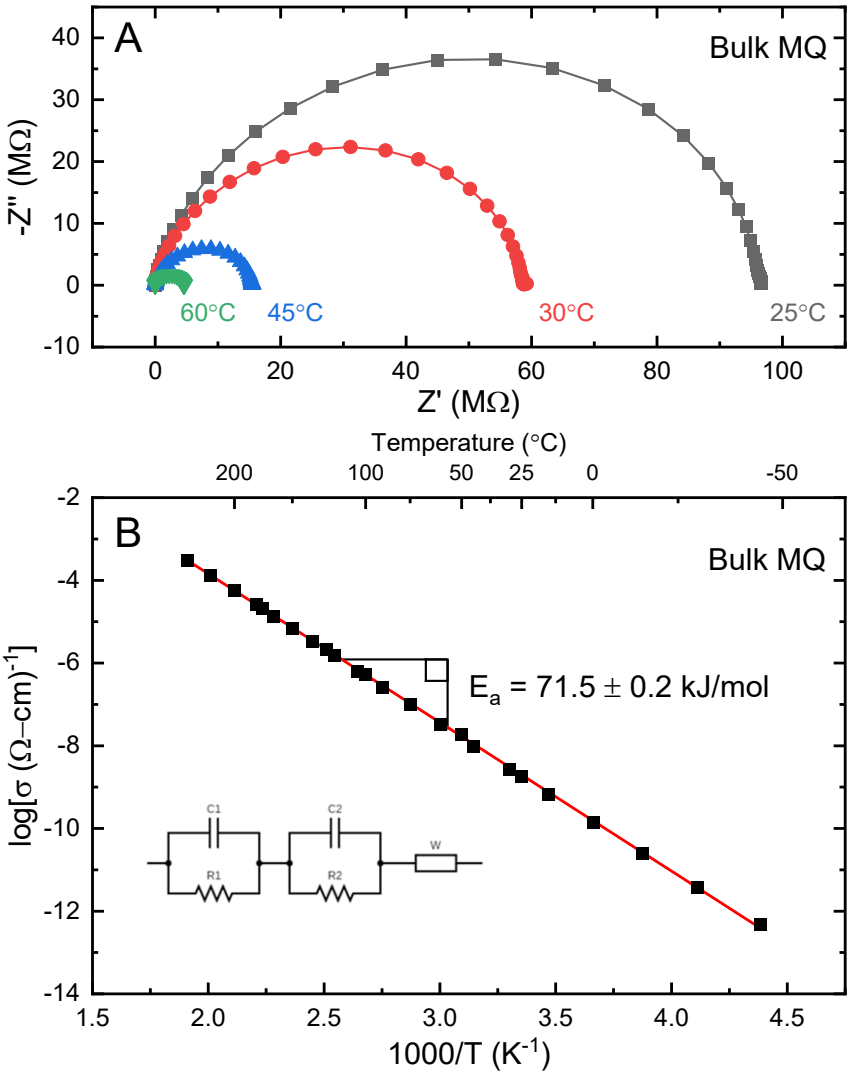

Figure 3. (a) Nyquist plot showing real and imaginary impedance for four temperatures of a bulk MQ 1.96 mm thick sample with 13 mm diameter gold sputtered electrodes. **(b)** Arrhenius plot showing the temperature dependent DC ionic conductivity of bulk MQ $LiPO_3$ GSSE, error bars are smaller than the symbol size.

Ionic Conductivity of Thin-film Cells

Symmetric cells of thin-film $LiPO_3$ GSSE were fabricated using LM foil electrodes. EIS scans were conducted at room temperature for ≈ 12 hours prior to conducting temperature-dependent

scans to determine the D.C. ionic conductivity. This hold period at room temperature is utilized to allow the interface between the lithium and the $LiPO_3$ GSSE to stabilize and to form more intimate contact. Time dependent Nyquist plots are shown in Figure 4a for a 90 μm thick sample, with equivalent circuit fitted resistance values shown in Figure 4b. The interfacial resistance tends to decrease over time before stabilizing. Based on reports from Wang *et al.*[45] and LePage *et al.*[46], it is believed that voids between the glass and the LM increase the interfacial impedance of the glass, and creep of the LM can help to fill these voids. Due to the low pressure that is used to apply the LM to the thin film, it is believed that voids are present during the initial formation of the cell, leading to a high interfacial impedance. As the LM creeps into these voids, the interfacial resistance decreases substantially. Following the first EIS scans at room temperature to reduce the voids, the cells were moved into the cryostat for temperature dependent EIS.

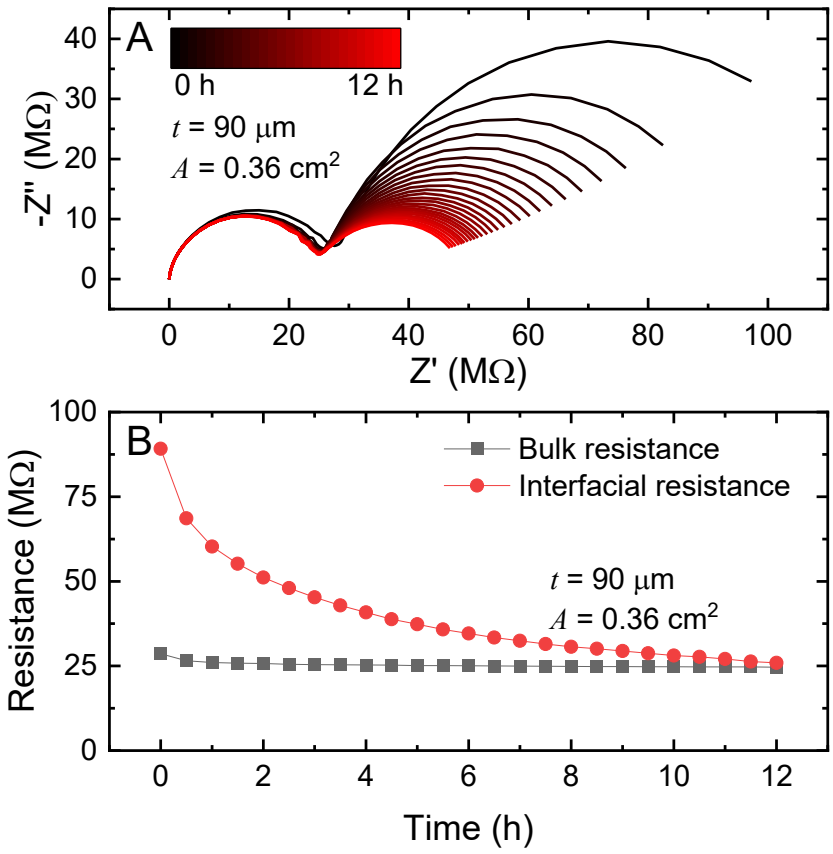

Figure 4. (a) Nyquist plot for LM | $LiPO_3$ | LM symmetric cell with electrolyte thickness of 90 μm after fabrication and scanned every thirty minutes for 12 hours. **(b)** Equivalent circuit fitted resistance values for the Nyquist plots shown in (a), showing a decreasing interfacial resistance with time with a relatively stable bulk impedance.

Modeling Resistance as a Function of Thickness and Temperature

The conductivity data determined above was used to develop the model in Figure 5b showing the ASR as a function of the thickness and temperature through a modified combination of Eqs. (3) and (4), shown in Eq. (5). Consistent with the Raman spectra showing no structural changes, it was assumed that no conductivity changes would occur during the drawing process and, thus, the resistance decreases linearly with decreasing electrolyte thickness. Thus, in decreasing the electrolyte thickness from 1 mm to 50 μm, the total resistance decreases 20-fold to 5% of the

original value, assuming no change in conductivity occurs during the film drawing process. The thickness values in the plot were chosen for comparison to the experimental thicknesses used to confirm the model. Film thicknesses ranging from 50 μm up to 610 μm were drawn and assembled into symmetric cells. EIS was conducted and resistance values were fitted using the same equivalent circuit diagram shown in Figure 3b. These experimental resistance values were normalized to ASR, with three thicknesses shown in Figure 5b. Plots of the ASR model and experimental results for thickness values between these three can be found in Figures S3 and S4. Comparison between the real and expected curves show that the real resistance behavior follows closely to the expected behavior, and further analysis of the data shows that the conductivity is not affected largely by film thickness, shown in the Arrhenius plot in Figure 5a. The conductivity of each thickness of thin film tested was calculated and shown at room temperature in Figure S5. Variations in conductivity may mostly be attributed to imperfect electrode contact leading to decreased contact area between the electrolyte and the LM. The validity of the model is assessed in Figure 5c, where the ratio, $\delta(T)$, of the logarithm of the real ASR of each thickness at various temperatures is compared to the logarithm of the expected ASR through Eq. (6).

$$ASR_{\text{model}}(T) = \mathrm{R}(T)A = \frac{t}{\sigma(T)} = \frac{t}{\frac{\sigma_0}{T}\exp\left(\frac{-\Delta E_a}{RT}\right)} \ [\Omega\text{-cm}^2] \quad \text{Eq. (5)}$$

$$\delta(T) = \log(ASR_{actual}(T)) / \log(ASR_{model}(T)) \quad \text{Eq. (6)}$$

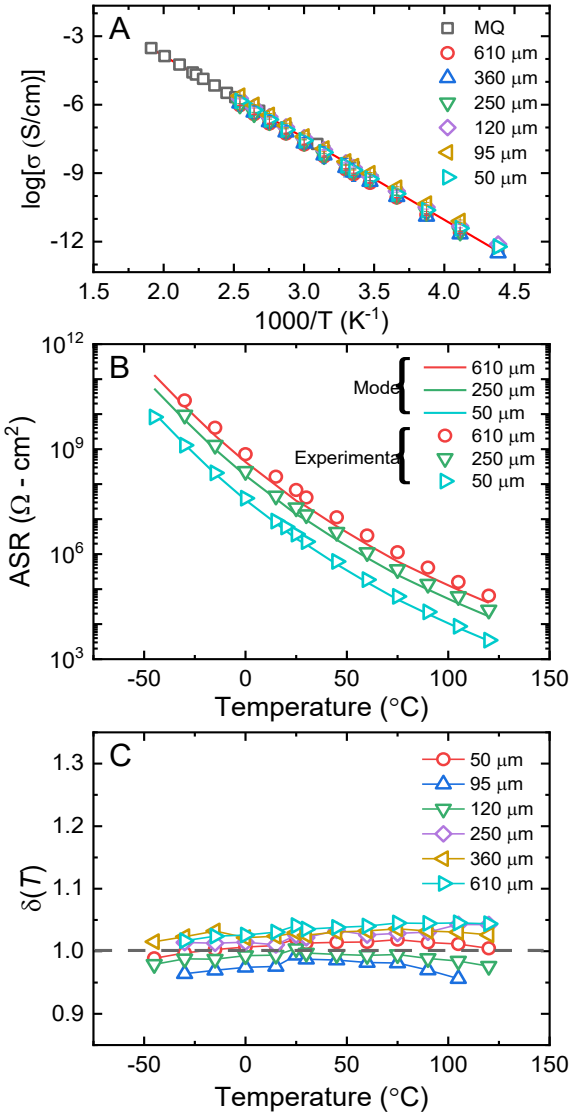

Figure 5. (a) Arrhenius plot of conductivity for a range of film thicknesses as a function of temperature compared to that of bulk MQ $LiPO_3$. **(b)** Symmetric cell measured ASR as a function of temperature for three different thicknesses of drawn thin films. **(c)** δ(T) ratio of measured ASR over the modeled ASR for validation of the model.

Calculated values of $\delta(T)$ close to 1.0 show the experimental results are in good agreement with values generated from the temperature-dependent ASR model. As Figure 5c shows, the values of $\delta(T)$ are centered near 1.0, with some minor fluctuations attributed to the actual contact area of

the lithium foil electrodes being different from the nominal area utilized for the calculation from resistance to ASR.

Symmetric Cell Cycling

Low current density, < 50 μA/cm^2, cycling was conducted on samples of thin films in the range of about 50 μm. After the coin cells were fabricated, EIS scans were conducted for four hours to characterize change in interfacial impedance. Following this four-hour period, galvanostatic cycling was conducted at room temperature, 60°C and 90°C. Due to the low conductivity of the $LiPO_3$ GSSE, low current densities were utilized to prevent the potentiostat from reaching its voltage limit (±10 V). Figure 6 shows the cycling profile at room temperature for 20 cycles with 15-minute charge/discharge cycles followed by 80 cycles with 2-hour charge/discharge cycles at constant current density of 0.1 μA/cm^2. The voltage required to produce the same current lowered over time, indicating a decrease in interfacial resistance. It is important to note that the wavelike behavior of the overpotential present from 100 hours on was due to small temperature fluctuations in the lab aggravated by the relatively high activation energy of this poor ion conductor. Due to the Arrhenius behavior of the conductivity and the high activation energy, small temperature changes lead to large changes in voltage to generate the same current.

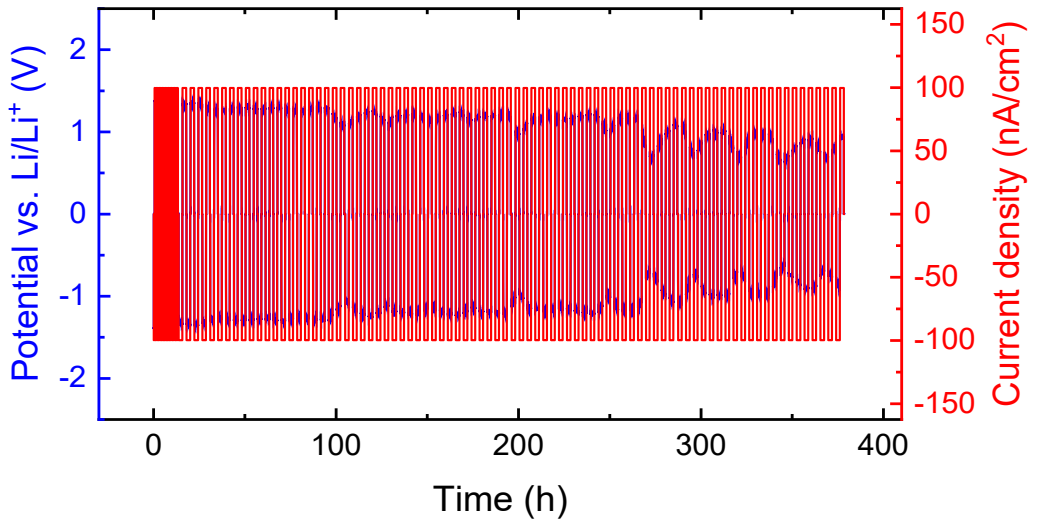

Figure 6. Galvanostatic cycling at 100 nA/cm^2 for 100 cycles for a 50 μm thick electrolyte with an area of ≈ 0.18 cm^2. Overall lowering of potential indicates that the interfacial layer is decreasing in resistance over time. Varying overpotentials after 200 hours are attributed to conductivity changes due to varying lab temperatures and a high activation energy.

Following cycling at room temperature, the cell was moved into an oven heated to 60°C and step increased current density testing was conducted. The cell was wrapped in insulation and left for 24 hours to allow the interior of the cell to reach 60°C. Current densities ranging from 1 to 5 μA/cm^2 were tested with 20 charge/discharge cycles of each value. As can be seen in Figure 7a, the cycling behavior for all of these current densities was very consistent, with no fluctuations in the overpotential. Following this, the temperature of the oven was increased to 90°C and the cell was left to equilibrate for another 24 hours, and the same test was conducted. As shown in Figure 7b, the cycling behavior at 90°C is nearly identical to that of the 60°C, but with a lower driving potential due to the increased conductivity of the thin-film $LiPO_3$ GSSE. A step-wise increased current density test was conducted to determine the CCD of the cell as fabricated with 6 cycles per current density and a constant amount of charge being transported during each cycle at the varying current densities. The cycling behavior seen in Figure 7c of the cell during the CCD test was once

again consistent and indicative of very little resistance change in the cell during cycling. Current densities up to 15 $\mu A/cm^2$ were tested and exhibited very stable cycling for each. The cell shorted at a current density of approximately 65 $\mu A/cm^2$, as shown in Figure 7d. The cell short circuit may be attributed to lithium dendrite growth through a defect in the GSSE surface leading to crack propagation and eventual mechanical fracture of the thin-film material after more than 350 cycles. The surface of the thin-film glass may retain some surface imperfections due to chill-marks present in the preform from quenching on a brass plate. Further, any bubbles in the preform will remain in the glass film during the drawing process. While neither of these are present in large quantities in the film, they are present in small proportions and may have served as the initiation site of the failure of the glass. It is believed that further improvement in reduction of defects, and more conformal lithium coating through techniques such as lithium evaporation would lead to a higher CCD than that reported here.

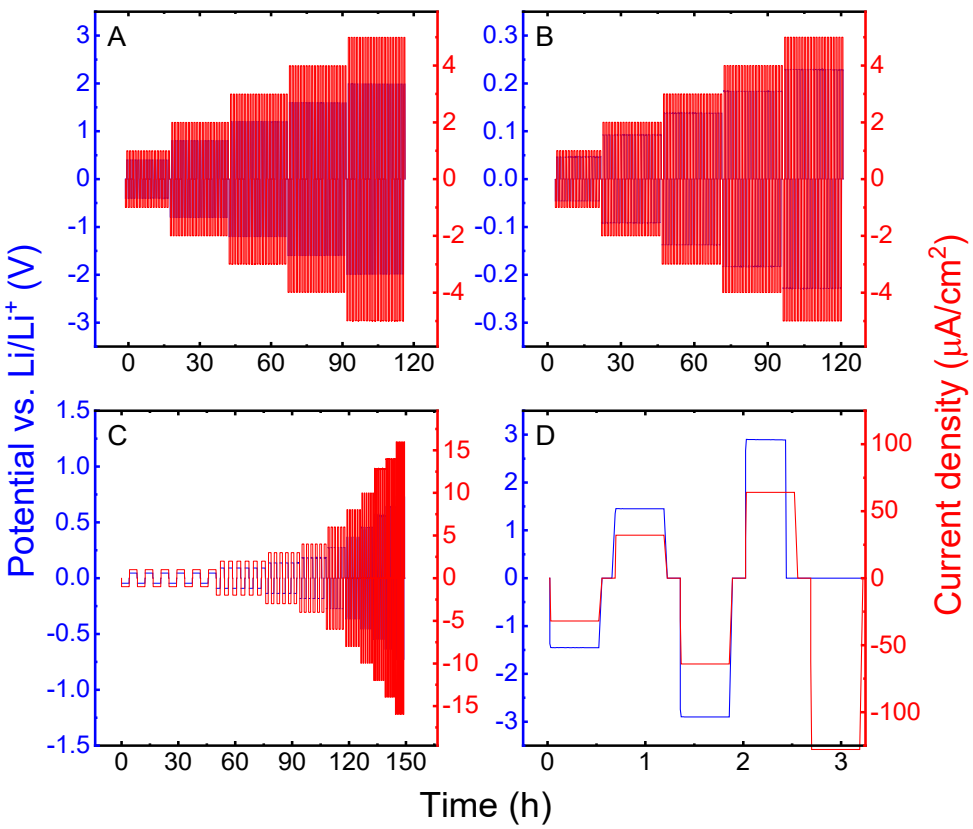

Figure 7. Step-increased current density testing of a 50 μm thin-film symmetric cell **(a)** at 60°C, **(b)** 90°C. CCD testing of a 50 μm thin film at 90°C with constant capacity **(c)** up to 15 μA/cm^2, (d) up to 65 μA/cm^2.

Conclusion

In this study, we report the first drawn thin-film GSSE. While exhibiting a lower conductivity, $LiPO_3$ oxide GSSE was used in our first attempt to draw glassy thin films due to its stability and ease-of-handling. In this report, we examined the conductivity, electrochemical, and cycling behaviors of drawn thin-film $LiPO_3$ GSSEs. Our work here shows that drawn thin-film GSSEs are a viable and easily scalable method of producing thin-film SSEs for use in high energy density LM secondary batteries. Thin glassy films of $LiPO_3$ can be easily drawn to thicknesses of

less than 50 μm. We examined a range of thicknesses from 50 μm for thin-film $LiPO_3$ up to 610 μm and found that the D.C Li ion conductivity of the thin films over this wide range of thicknesses agreed extremely well with our measurements of the bulk MQ $LiPO_3$ GSSE from -50 to + 275ºC. Our value of the RT conductivity for both films and bulk MQ GSSE further agreed well with reported literature values. For a 50 μm thin-film $LiPO_3$ GSSE with a conductivity of $10^{-6.5}$ $[\Omega\text{-cm}]^{-1}$ at 90ºC, it demonstrated stable and reversible cycling with no lithium dendrite penetration at current densities less than about 65 $\mu A/cm^2$. Stable cycling at room temperature and elevated temperatures were demonstrated for greater than 350 total cycles and over 800 hours. Drawn thin-film GSSEs represent an entirely new synthesis and processing technique for thin ionically conductive SSEs and further study is required to investigate this technique for more highly conductive glass chemistries.

ASSOCIATED CONTENT

Supporting Information.

The following files are available free of charge.

Supplemental information contains a figure showing a DSC thermogram for $LiPO_3$, the Raman spectra and peak assignments, and three figures showing area specific resistance and conductivity data for the generated model and the experimental data for more thickness values.

Corresponding Author

*Steve W. Martin: swmartin@iastate.edu, Phone: 515-294-0745

Author Contributions

The manuscript was written through contributions of JW, SK, DS, CS, and SM. All authors have given approval to the final version of the manuscript. Thin film was synthesized and drawn by DS and CS. Other experiments were designed by JW and SK and carried out by JW.

Funding Sources

DOE EERE VTO DE-EE0008852

NASA EPSCoR 80NNSSC20M0219

ACKNOWLEDGEMENTS

Funding for this work was provided by the Vehicle Technologies Office of the EERE office of the Department of Energy through contract number DE-EE0008852 and from the NASA EPSCoR program through contract number 80NNSSC20M0219.

ABBREVIATIONS

GSSE, glassy solid-state electrolyte; EIS, electrochemical impedance spectroscopy; ASR, area specific resistance; SSE, solid-state electrolyte; MQ, melt-quenched; BO, bridging oxygen; NBO, non-bridging oxygen.

REFERENCES

1. Gallo, A. B.; Simões-Moreira, J. R.; Costa, H. K. M.; Santos, M. M.; Moutinho dos Santos, E., Energy storage in the energy transition context: A technology review. *Renewable and Sustainable Energy Reviews* **2016,** *65*, 800-822.

2. Zubi, G.; Dufo-López, R.; Carvalho, M.; Pasaoglu, G., The lithium-ion battery: State of the art and future perspectives. *Renewable and Sustainable Energy Reviews* **2018,** *89*, 292-308.

3. Tarascon, J. M.; Armand, M., Issues and challenges facing rechargeable lithium batteries. *Nature (London, United Kingdom)* **2001,** *414* (6861), 359-367.

4. Ozawa, K., Lithium-ion rechargeable batteries with LiCoO2 and carbon electrodes: the LiCoO2/C system. *Solid State Ionics* **1994,** *69* (3), 212-221.

5. Whittingham, M. S., Lithium Batteries and Cathode Materials. *Chemical Reviews (Washington, DC, United States)* **2004,** *104* (10), 4271-4301.

6. Yoshino, A., The Birth of the Lithium-Ion Battery. *Angewandte Chemie International Edition* **2012,** *51* (24), 5798-5800.

7. Goodenough, J. B.; Park, K.-S., The Li-Ion Rechargeable Battery: A Perspective. *Journal of the American Chemical Society* **2013,** *135* (4), 1167-1176.

8. Scrosati, B., History of lithium batteries. *Journal of Solid State Electrochemistry* **2011,** *15* (7), 1623-1630.

9. Nishi, Y., Lithium ion secondary batteries; past 10 years and the future. *Journal of Power Sources* **2001,** *100* (1), 101-106.

10. Barrow, C. S.; Lucia, H.; Stock, M. F.; Alarie, Y., Development of methodologies to assess the relative hazards from thermal decomposition products of polymeric materials. *American Industrial Hygiene Association Journal* **1979,** *40* (5), 408-423.

11. Levy, S. C., Safety and reliability considerations for lithium batteries. *Journal of Power Sources* **1997,** *68* (1), 75-77.

12. Nitta, N.; Wu, F.; Lee, J. T.; Yushin, G., Li-ion battery materials: present and future. *Materials Today* **2015,** *18* (5), 252-264.

13. Xia, S.; Wu, X.; Zhang, Z.; Cui, Y.; Liu, W., Practical Challenges and Future Perspectives of All-Solid-State Lithium-Metal Batteries. *Chem* **2019,** *5* (4), 753-785.

14. Kerman, K.; Luntz, A.; Viswanathan, V.; Chiang, Y.-M.; Chen, Z., Review—Practical Challenges Hindering the Development of Solid State Li Ion Batteries. *Journal of The Electrochemical Society* **2017,** *164*, A1731-A1744.

15. Chen, C. H.; Xie, S.; Sperling, E.; Yang, A. S.; Henriksen, G.; Amine, K., Stable lithium-ion conducting perovskite lithium–strontium–tantalum–zirconium–oxide system. *Solid State Ionics* **2004,** *167* (3), 263-272.

16. Wu, J.; Yuan, L.; Zhang, W.; Li, Z.; Xie, X.; Huang, Y., Reducing the thickness of solid-state electrolyte membranes for high-energy lithium batteries. *Energy & Environmental Science* **2021,** *14* (1), 12-36.

17. Xu, R. C.; Xia, X. H.; Zhang, S. Z.; Xie, D.; Wang, X. L.; Tu, J. P., Interfacial challenges and progress for inorganic all-solid-state lithium batteries. *Electrochimica Acta* **2018,** *284*, 177-187.

18. Han, F.; Westover, A. S.; Yue, J.; Fan, X.; Wang, F.; Chi, M.; Leonard, D. N.; Dudney, N. J.; Wang, H.; Wang, C., High electronic conductivity as the origin of lithium dendrite formation within solid electrolytes. *Nature Energy* **2019,** *4* (3), 187-196.

19. Schafbauer, W.; Schulze-Küppers, F.; Baumann, S.; Meulenberg, W. A.; Menzler, N. H.; Buchkremer, H. P.; Stöver, D., Tape Casting as a Multi Purpose Shaping Technology for Different Applications in Energy Issues. *Materials Science Forum* **2012,** *706-709*, 1035-1040.

20. Rabin, B. H., Modified Tape Casting Method for Ceramic Joining: Application to Joining of Silicon Carbide. *Journal of the American Ceramic Society* **1990,** *73* (9), 2757-2759.

21. Minami, K.; Mizuno, F.; Hayashi, A.; Tatsumisago, M., Lithium ion conductivity of the Li2S-P2S5 glass-based electrolytes prepared by the melt quenching method. *Solid State Ionics* **2007,** *178* (11-12), 837-841.

22. Nishihora, R. K.; Rachadel, P. L.; Quadri, M. G. N.; Hotza, D., Manufacturing porous ceramic materials by tape casting—A review. *Journal of the European Ceramic Society* **2018,** *38* (4), 988-1001.

23. Tatsumisago, M.; Hayashi, A., Superionic glasses and glass-ceramics in the Li2S-P2S5 system for all-solid-state lithium secondary batteries. *Solid State Ionics* **2012,** *225*, 342-345.

24. Minami, T.; Machida, N., Preparation of new glasses with high ionic conductivities. *Solid State Ionics, Proc.Symp.A2 Int.Conf.Adv.Mater.* **1992**, 91-102.

25. Kennedy, J. H.; Zhang, Z.; Eckert, H., Ionically conductive sulfide-based lithium glasses. *J.Non-Cryst.Solids* **1990,** *123, 328-38*.

26. Zhao, R.; Kmiec, S.; Hu, G.; Martin, S. W., Lithium Thiosilicophosphate Glassy Solid Electrolytes Synthesized by High-Energy Ball-Milling and Melt-Quenching: Improved Suppression of Lithium Dendrite Growth by Si Doping. *ACS applied materials & interfaces* **2020,** *12* (2), 2327-2337.

27. Kmiec, S. J.; Lovi, J. M.; Joyce, A.; Bayko, D.; Martin, S. W., Anomalously strong viscosity behavior in mixed oxy-sulfide Na4P2S7-xOx invert glasses. *Journal of Non-Crystalline Solids* **2021,** *553*, 120493.

28. Glass, A. M.; Nassau, K., Lithium ion conduction in rapidly quenched Li2O-Al2O3, Li2O-Ga2O3, and Li2O-Bi2O3 glasses. *Journal of Applied Physics* **1980,** *51* (7), 3756-3761.

29. Ravaine, D., Glasses as solid electrolytes. *J.Non-Cryst.Solids* **1980,** *38-39*, 353

-358.

30. Levasseur, A.; Olazcuaga, R.; Kbala, M.; Zahir, M.; Hagenmuller, P.; Couzi, M., Etudes electrique et Raman des verres des systemes B2O3□M2O□M3PO4 (M=Li, Na). *Solid State Ionics* **1981,** *2* (3), 205-213.

31. Pradel, A.; Ribes, M., Electrical properties of lithium conductive silicon sulfide glasses prepared by twin roller quenching. *Solid State Ionics* **1986,** *18-19, 351-5*.

32. Kennedy, J. H., Ionically conductive glasses based on silicon disulfide. *Mater.Chem.Phys.* **1989,** *23, 29-50*.

33. Meyer, B.; Borsa, F.; Martin, S. W., Structure and properties of lithium thio-boro-germanate glasses. *Journal of Non-Crystalline Solids* **2004,** *337* (2), 166-173.

34. Mizuno, F.; Hayashi, A.; Tadanaga, K.; Minami, T.; Tatsumisago, M., All-solid-state lithium secondary batteries using Li2S-SiS2-Li4SiO4 glasses and Li2S-P2S5 glass ceramics as solid electrolytes. *Solid State Ionics* **2004,** *175* (1-4), 699-702.

35. Zhao, R.; Hu, G.; Kmiec, S.; Gebhardt, R.; Whale, A.; Wheaton, J.; Martin, S. W., New Amorphous Oxy-Sulfide Solid Electrolyte Material: Anion Exchange, Electrochemical Properties, and Lithium Dendrite Suppression via In Situ Interfacial Modification. *ACS applied materials & interfaces* **2021,** *13* (23), 26841-26852.

36. Albertus, P.; Anandan, V.; Ban, C.; Balsara, N.; Belharouak, I.; Buettner-Garrett, J.; Chen, Z.; Daniel, C.; Doeff, M.; Dudney, N. J.; Dunn, B.; Harris, S. J.; Herle, S.; Herbert, E.; Kalnaus, S.; Libera, J. A.; Lu, D.; Martin, S.; McCloskey, B. D.; McDowell, M. T.; Meng, Y. S.; Nanda, J.; Sakamoto, J.; Self, E. C.; Tepavcevic, S.; Wachsman, E.; Wang, C.; Westover, A. S.; Xiao, J.; Yersak, T., Challenges for and Pathways toward Li-Metal-Based All-Solid-State Batteries. *ACS Energy Letters* **2021,** *6* (4), 1399-1404.

37. Aotani, N.; Iwamoto, K.; Takada, K.; Kondo, S., Synthesis and electrochemical properties of lithium ion conductive glass, Li3PO4- Li2S - SiS2. *Solid State Ionics* **1994,** *68* (1-2), 35-39.

38. Money, B. K.; Hariharan, K., Lithium ion conduction in lithium metaphosphate based systems. *Applied Physics A* **2007,** *88* (4), 647-652.

39. Kartini, E.; Y. S. Panca Putra, T.; Kuntoro, I.; Sakuma, T.; Basar, K.; Kamishima, O.; Kawamura, J., Recent Studies on Lithium Solid Electrolytes (LiI)x(LiPO3)1-x for Secondary Battery. *Journal of the Physical Society of Japan* **2010,** *79* (Suppl.A), 54-58.

40. De Souza, J. E.; Rojas De Souza, S.; Gebhardt, R.; Kmiec, S.; Whale, A.; Warthen Martin, S., LiPON and NaPON glasses: A study of the ammonolysis of lithium and sodium metaphosphate melts. *International Journal of Applied Glass Science* **2020,** *11* (1), 78-86.

41. O'Kiely, D.; Breward, C. J. W.; Griffiths, I. M.; Howell, P. D.; Lange, U., Edge behaviour in the glass sheet redraw process. *Journal of Fluid Mechanics* **2015,** *785*, 248-269.

42. Wang, B.; Kwak, B. S.; Sales, B. C.; Bates, J. B., Ionic conductivities and structure of lithium phosphorus oxynitride glasses. *Journal of Non-Crystalline Solids* **1995,** *183* (3), 297-306.

43. Martin, S. W.; Angell, C. A., D.c. and a.c. conductivity in wide composition range lithium oxide-phosphorus oxide (Li2O-P2O5) glasses. *J.Non-Cryst.Solids* **1986,** *83* (1-2), 185-207.

44. Hockicko, P.; Kúdelčík, J.; Muñoz, F.; Muñoz-Senovilla, L., Structural and Electrical Properties of LiPO3 Glasses. *Advances in Electrical and Electronic Engineering* **2015,** *13*.

45. Wang, M. J.; Choudhury, R.; Sakamoto, J., Characterizing the Li-Solid-Electrolyte Interface Dynamics as a Function of Stack Pressure and Current Density. *Joule* **2019,** *3* (9), 2165-2178.

46. LePage, W. S.; Chen, Y.; Kazyak, E.; Chen, K.-H.; Sanchez, A. J.; Poli, A.; Arruda, E. M.; Thouless, M. D.; Dasgupta, N. P., Lithium Mechanics: Roles of Strain Rate and Temperature and Implications for Lithium Metal Batteries. *Journal of The Electrochemical Society* **2019,** *166* (2), A89-A97.

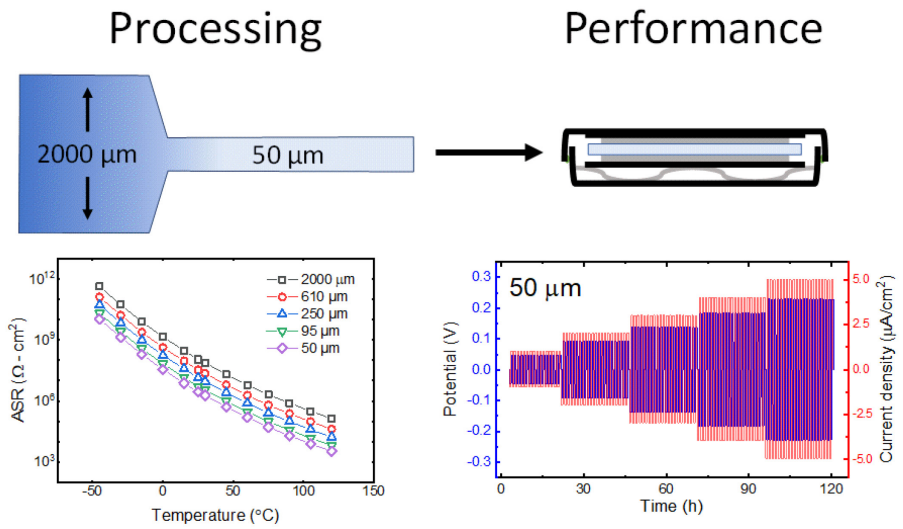
Processing
Performance
2000 µm
50 µm
ASR (Ω - cm²)
Temperature (°C)
2000 µm
610 µm
250 µm
95 µm
50 µm
50 µm
Potential (V)
Current density (µA/cm²)
Time (h)